scientific reports

OPEN

Efficient photocatalytic degradation of textile dye pollutants using thermally exfoliated graphitic carbon nitride (TE–g–C$_3$N$_4$)

Selvaganapathy Ganesan[1,2], Thangavelu Kokulnathan[3], Shanmugam Sumathi[1] & Arunkumar Palaniappan[2✉]

Graphitic carbon nitride (g–C$_3$N$_4$), an organic photocatalyst was reported to have beneficial properties to be used in wastewater treatment applications. However, g–C$_3$N$_4$, in its bulk form was found to have poor photocatalytic degradation efficiency due to its inherent limitations such as poor specific surface area and fast electron–hole pair recombination rate. In this study, we have tuned the physiochemical properties of bulk g–C$_3$N$_4$ by direct thermal exfoliation (TE–g–C$_3$N$_4$) and examined their photocatalytic degradation efficiency against abundant textile dyes such as methylene blue (MB), methyl orange (MO), and rhodamine B (RhB). The degradation efficiencies for MB, MO, and RhB dyes are 92 ± 0.18%, 93 ± 0.31%, and 95 ± 0.4% respectively in 60 min of UV light irradiation. The degradation efficiency increased with an increase in the exfoliation temperature. The prepared catalysts were characterized using FTIR, XRD, FE-SEM, EDAX, BET, and UV-DRS. In BET analysis, TE–g–C$_3$N$_4$ samples showed improved surface area (48.20 m^2/g) when compared to the bulk g–C$_3$N$_4$ (5.03 m^2/g). Further, the TE–g–C$_3$N$_4$ had 2.98 times higher adsorption efficiency than the bulk ones. The free radicals scavenging studies revealed that the superoxide radicals played an important role in the photodegradation for dyes, when compared to the hydroxyl radical ($\cdot$OH) and the photo-induced holes (h$^+$), Photoluminescence (PL) emission and electrochemical impedance spectroscopy (EIS) spectra of TE–g–C$_3$N$_4$ indicated a lowered electron–hole pairs' recombination rate and an increased photo-induced charge transfer respectively. Further, the TE–g–C$_3$N$_4$ were found to have excellent stability for up to 5 cycles with only a minor decrease in the activity from 92% to 86.2%. These findings proved that TE–g–C$_3$N$_4$ was an excellent photocatalyst for the removal and degradation of textile dyes from wastewater.

In recent years, globalization, the advancement of technology, coupled with the evolving fashion preferences of humans, has significantly contributed to the augmentation of textile and garment manufacturing[1,2]. Compared to the past decade, consumers buy clothes twice the time and keep them for only half the time[3]. This huge production of textile products and their shorter utilization creates dramatic textile and apparel waste after consumer usage. Also, these industries use synthetic pigments as coloring agents[4–6]. The textile and fashion industries are globally criticized for pernicious environmental impact (water contamination, waste generation, and carbon footprint) throughout their supply chain[7]. For example, The Ganga river in India experiences a daily influx of around 250 million liters of industrial effluent as a consequence of human encroachment in the surrounding regions[8–10]. The pigments used in the textile industries are stable, highly aqueous soluble, toxic, carcinogenic, and non-biodegradable[11,12]. These dyes obstruct the sunlight penetration range and result in reduced photosynthesis process which causes unavailability of oxygen to aquatic organisms. Moreover, the ingestion or inhalation of the

[1]Department of Chemistry, School of Advanced Sciences, Vellore Institute of Technology, Vellore, Tamil Nadu 632014, India. [2]Human Organ Manufacturing Engineering (HOME), Lab, Centre for Biomaterials, Cellular and Molecular Theranostics (CBCMT), Vellore Institute of Technology, Vellore, Tamil Nadu 632014, India. [3]Department of Electro-Optical Engineering, National Taipei University of Technology, Taipei 106, Taiwan. ✉email: arunkumar.p@vit.ac.in

toxic dyes is reported to trigger respiratory infections, skin, and eye irritations[13–15]. Also, some dyes are found to get converted into carcinogenic compounds in anaerobic conditions, thus leads to the manifestation of various health conditions, including but not limited to cancer, asthma, diarrhea, nausea, and diverse forms of allergic reactions[16,17]. The most widely used methods for the removal of these hazardous dyes are adsorption, biosorption, filtration, ion exchange, coagulation, and advanced oxidation process (AOP)[18–20]. In recent times, AOP-based photocatalytic wastewater treatment methods have been widely used for environmental depollution due to their advantages such as eco-friendliness, low maintenance cost, easier operation, and high efficiency[21–23]. The photocatalysts are typically semiconductor materials that generate electron–hole pair upon irradiation with light source. This in turn reacts with dissolved oxygen and moisture present in the dye solution to produce reactive ion species. These reactive ion species then convert toxic organic dyes to non-toxic or secondary pollutants[24,25]. Several metal oxides, noble metals, metal carbides, and sulfur-based semiconductors are used as photocatalysts to remove pollutants from the environment[26,27]. However, these metal-based photocatalytic materials have limitations such as high cost, low quantum efficiency, lower availability, and more importantly generation of metallic pollutants when these catalysts are discarded. This leads to a scenario where treatment strategies and components polluting back the environment. Thus, there is a strong need for a metal-free catalyst with better photocatalytic efficiency[28].

Graphitic carbon nitride (g–C$_3$N$_4$) is one such metal-free semiconductor with an excellent physico-chemical and photocatalytic properties. The electrons generated through photoexcitation in g–C$_3$N$_4$ exhibited a higher thermodynamic potential to facilitate the reduction of diverse organic compounds into H$_2$O and CO$_2$[29,30]. However, g–C$_3$N$_4$ in its bulk form had several drawbacks, such as a limited specific surface area and an accelerated recombination rate[31,32] There are reports in the literature where the photocatalytic performance of bulk g–C$_3$N$_4$ were increased by making composites with metal oxides, quantum dots, and fabricating heterojunction structures[33–37]. However, in the above methods, g–C$_3$N$_4$ was typically combined with other materials using multi-step reactions, which increased the cost as well as the complexity. Thus, exfoliation of g–C$_3$N$_4$ using physical methods (e.g. thermal treatment) or chemical methods (e.g. acid etching) was an attractive option to improve their photocatalytic performances, mainly through the enhancement in their surface area due to the formation of this and porous structures. Various researchers have made highly porous and sheet-like g–C$_3$N$_4$ for enhanced photocatalytic performance through protonated exfoliation or hydrothermal breakdown; however, these procedures were complex and expensive[38–40]. Among them, thermal exfoliation was the most environment-friendly option which was currently being explored.

The thermal exfoliation process of g–C$_3$N$_4$ was a straightforward method for the synthesis of a catalyst that exhibited an excellent porosity and efficiency, making it suitable for many environmental applications (Fig. 1). From the previously published literature, thermal exfoliation of g–C$_3$N$_4$ was synthesized by various researchers with different precursors and parameters for applications such as NOx removal and H$_2$ production[41–44]. In the present work, we reported the preparation of g–C$_3$N$_4$ by thermal exfoliation at static air and examined its adsorption and photocatalytic degradation efficiency against the most common textile dyes such as methylene blue (MB), methyl orange (MO), and rhodamine B (RhB) dye solutions under UV light irradiations. Finally, we have also investigated the mechanisms through which these thermally exfoliated photocatalysts degraded the dyes using radical scavenging experiments as well as by calculating the band potentials to confirm the active species involved in the reaction. To the best of our current understanding, there is a lack of documented research pertaining to the photodegradation of textile dyes by the utilization of TE–g–C$_3$N$_4$ using UV light irradiation, which we have addressed through this work.

Experimental section
Materials
Melamine (C$_3$H$_6$N$_6$) $\geq$ 98% was purchased from SD Fine Chemicals Ltd, Mumbai, India. Methylene blue (MB) (C$_{16}$H$_{18}$ClN$_3$S), rhodamine B (RhB) (C$_{28}$H$_{31}$ClN$_2$O$_3$), methyl orange (MO) (C$_{14}$H$_{14}$N$_3$NaO$_3$S), ammonium
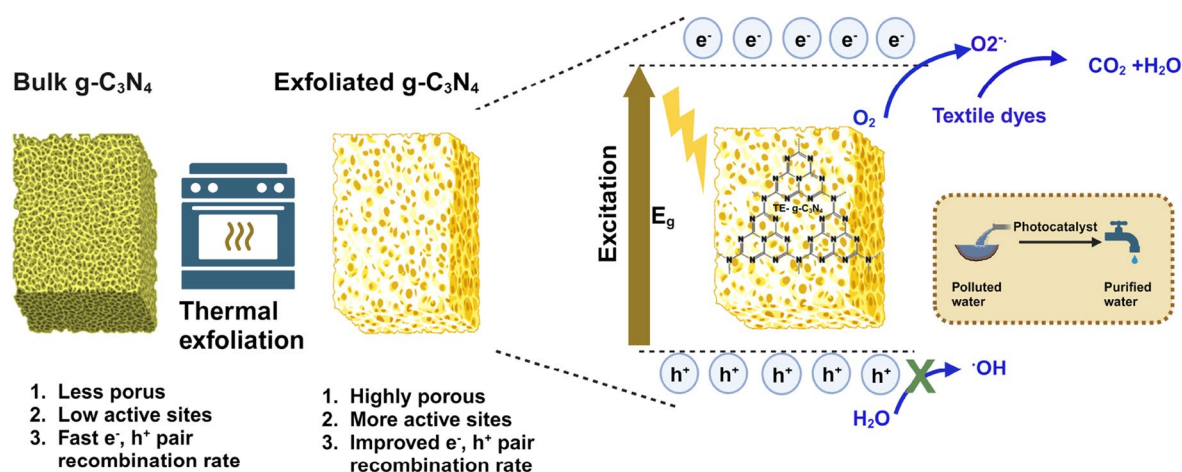

Figure 1. Schematic showing the preparation of TE–g–C$_3$N$_4$ and its photocatalytic mechanism.

oxalate ($C_2H_8N_2O_4$) ≥ 99%, and isopropyl alcohol (IPA) (C_3H_8O) ≥ 99.5%, potassium chloride (KCL) 99.5%, were purchased from SRL Chemical, Mumbai; para-benzoquinone (P–BQ) ($C_6H_4O_2$) ≥ 98%, sodium sulfate (Na_2SO_4) ≥ 99%, was purchased from Sigma Aldrich, Bengaluru. All chemicals employed in the study were of analytical pure grade and were utilized without undergoing additional purification processes. All studies were conducted using Milli-Q water.

Synthesis

Preparation of bulk g–C₃N₄

The bulk g-C_3N_4 was synthesized using melamine as per protocol[45]. In a concise manner, a quantity of 10 g of melamine was placed into a sealed crucible made of alumina. The temperature of the crucible was raised to 550 °C at 5 °C per minute. The sample was kept in the above condition for 4 h in the static air, after which samples were cooled down to obtain yellow-colored agglomerates. The agglomerates were then ground to get fine powders using agate mortar.

Preparation of TE–g–C₃N₄

TE–g–C_3N_4 samples were synthesized using the process of heating pre-existing bulk g–C3N4 material within an open alumina crucible, employing various temperature condition of 450 °C, 500 °C, and 550 °C for 2 h with a rate of 5 °C per min. The resultant samples were labelled as g–C_3N_4 450, g–C_3N_4 500, g–C_3N_4 550 corresponding to 450 °C, 500 °C, and 550 °C respectively.

Characterization

X-ray diffraction (XRD) tests were employed to verify the production and purity of the synthesized materials using Panalytical X'Pert[3]. The characteristic functional groups present in the synthesized materials were identified using Agilent Cary 630 Fourier transform infrared (FTIR) spectroscopy [Agilent Cary 630] studies. The analysis of the samples' surface area was conducted using the Brunauer–Emmett–Teller (BET) technique using Bellsorp Max II analyzer. Surface morphology and elemental analysis of all the materials were examined by field emission scanning electron microscope (FESEM)-Thermo Fisher FEI-Quanta 250 FEG. JASCO V-670 UV–Vis–NIR spectrophotometer was used to obtain the optical properties such as absorbance spectra and band gap. The concentration of the remnant dyes present in the system after a photodegradation experiment was detected using a UV–Vis spectrophotometer (Agilent Cary 3500). Photoluminescence (PL) properties of the materials were investigated with a HITACHI F-7000 fluorescence spectrophotometer.

Photocatalytic experiments

The photocatalytic activity of the TE–g–C_3N_4 samples was investigated using most abundantly used organic textile dyes: MB, RhB, and MO as per the protocol in the literature[46]. Briefly, 0.05% w/v of the TE–g–C_3N_4 sample was added into 50 mL dye solutions (10 ppm) and stirred for 30 min in dark conditions to attain adsorption/desorption equilibrium. Subsequently, the samples underwent additional agitation within a photoreactor while being exposed to UV light (with a wavelength of 365 nm and power output of 125 W), in order to assess the catalysts' ability to degrade the dye. At discrete time intervals, a 3 mL aliquot was extracted from the solution and subjected to centrifugation in order to isolate the catalyst. The amount of dye in the solution was quantified using a UV–Vis spectrophotometer. The adsorption and degradation efficiency of dyes were determined using the absorbance maxima peaks exhibited by the dyes: MB-664 nm, RhB-554 nm, and MO-464 nm in the absence and presence of light irradiation. The radical scavenging studies were performed with the best performing catalyst, g–C_3N_4 550 against all three dyes. The experimental procedure involved the addition of specific trapping agents, namely ammonium oxalate (AO), isopropyl alcohol (IPA), and para-benzoquinone (P–BQ), in order to scavenge the photogenerated holes (h^+), hydroxyl radicals (·OH), and superoxide radicals ($O_2^{·-}$) species, respectively.

The degradation percentage of each dye and the rate constant of the photocatalyst reaction were evaluated using the following equations.

$$\text{Degradation percentage}: 1 - [C/C_0] \times 100 \tag{1}$$

$$\text{Pseudo first order reaction kinetics}: \ln C_0/C = kt \tag{2}$$

where, C—Concentration of dye at time t, C_0—Initial concentration of the dye at t = 0, k—Rate constant s^{-1}.

Electrochemical measurements

Mott-Schottky analysis was performed to confirm the conduction band value. Using 0.5 M Na_2SO_4 as an electrolyte solution, Ag/AgCl as the reference electrode, and platinum as the counter electrode with fixed frequency of 1 kHz. EIS analysis was carried out to determine the charge transfer ability of the catalyst using solution containing 5 mM [Fe $(CN)_6$]$^{3-/4-}$ and 0.1 M KCl. For electrode fabrication, 10 mg/mL of catalyst was uniformly dispersed using bath sonicator for 30 min. After sonication, 8μL of homogenous solution was drop casted on screen printed electrode (SPCE) and dried at room temperature.

Results and Discussion

Powder XRD results

Figure 2a showed the XRD pattern of all the prepared g–C_3N_4 samples. All the samples exhibited a similar XRD pattern that matches with JCPDS No. 87-1526, which corresponds to graphitic carbon nitride[47]. The diffraction pattern exhibited two prominent peaks at around ~ 27° (002) and ~ 12° (100), indicating the structural

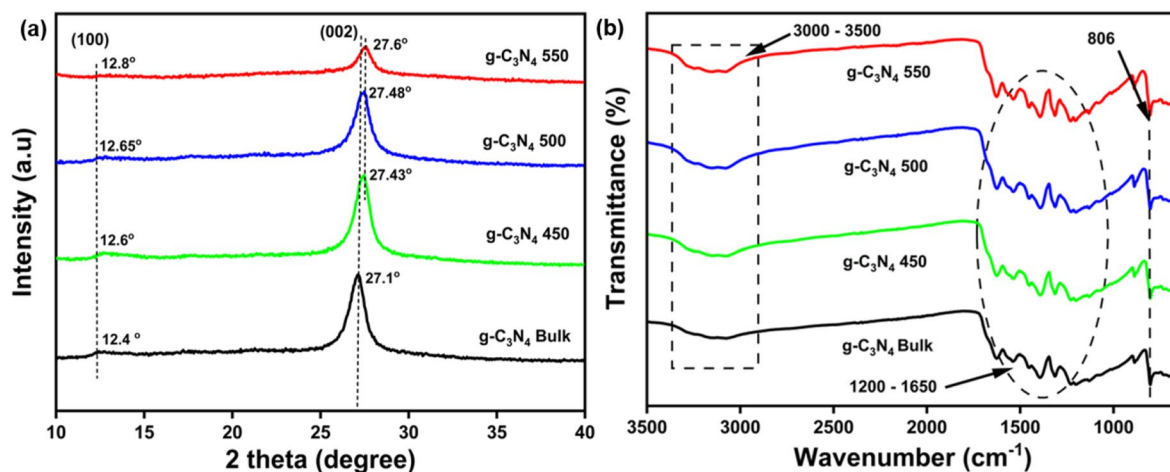**Figure 2.** (**a**) Powder XRD results of g–C₃N₄ Bulk, g–C₃N₄ 450, g–C₃N₄ 500, g–C₃N₄ 550, (**b**) FTIR spectra of the prepared samples.

arrangement of tri-s-triazine heterocycles and the periodic repetition of heptazine units inside the plane, respectively. The thermally exfoliated samples showed broader peaks with reduced intensities when compared to their bulk counterparts, which probably depicted the reduced layer spacing in the exfoliated ones[48]. Thus, (002) peak strength of the samples steadily decreased, indicating a comparable exfoliation of the g–C₃N₄. The reduction in peak intensities, was associated with decrease in crystallinity with increase in surface area and porosity. The surface area and porosity are two key factors responsible for an efficient photocatalyst[49]. Moreover, higher angular shifts for the thermally exfoliated g–C₃N₄ samples [g–C₃N₄ 450 (12.6°) (27.43°), g–C₃N₄ 500 (12.65°) (27.48°), g–C₃N₄ 550 (12.8°) (27.6°)] when compared to the bulk one [g–C₃N₄ bulk (12.4°) (27.1°)] could again be attributed to the reduced interlayer spacing[50]. The crystallite size of the sample was calculated using Scherrer formula: $D = K\lambda/\beta\cos\theta$, where D is crystallite size in (nm), β represents the full-width-at-half-maximum for the peak of the (101) plane, λ represents the wavelength of the X-ray radiation (0.15418 nm), and K is the Scherrer constant, which is assumed to have a value of 0.9[51]. The calculated crystallite size of the as prepared catalyst is listed in Table 1.

FTIR analysis

Functional groups and chemical bonding of prepared materials were studied by Fourier transform infrared (FTIR) spectroscopy, as shown in Fig. 2b. Here all the prepared samples possess similar characteristics spectra of g–C₃N₄. The typical peaks attributed to g–C₃N₄ were present in all the samples prepared. The sharp peak observed at 806 cm⁻¹ was attributed to the breathing mode of tri-s-triazine heterocycles. Moreover, the bands observed at 3000–3500 cm⁻¹ depicted the stretching of O–H/N–H motifs in samples originating from the surface NH/NH₂ groups and adsorbed water molecules[52,53]. In particular, the region from 1200 to 1650 cm⁻¹ corresponds to the stretching vibrations of N–(C)₃ and N=C heterocycles[54,55]. Finally, the similarity among the sample's band stretching suggests that the thermal exfoliation does not make any significant changes in the g–C₃N₄[56].

XPS analysis

The XPS analysis was performed to analyze the detailed chemical status of the catalyst prepared. As observed from Fig. 3a, the C 1s spectrum of bulk g–C₃N₄ fitted into binding energies of 288.2 eV and 284.9 eV, which can be attributed to the graphitic sites present in the g–C₃N₄ matrix of SP²-hybridized carbon atom bonded to N in the aromatic ring (N–C=N), SP² C=C bonds and C–NH₂ bonds respectively. The spectra of bulk g–C₃N₄ N 1s in Fig. 3b also showed the fitted binding energy peaks of 398.7 eV and 400.15 eV which are attributed to the SP² hybridized C=N–C bond in the triazine ring and N–(C)₃ bonds [57,58]. The XPS spectrum of g–C₃N₄ 550 C1 s and N1 s are shown in Figs. 3c, d. The (N–C=N) and (C=C) bonds' binding energy peaks in the C 1s spectra

Sample	Surface area m²/g	Pore volume (cm³/g)	Crystallite size (nm)	Band gap (eV)	Elemental composition	
					C (wt%)	N (wt%)
g–C₃N₄ Bulk	5.035	0.028	9.0	2.54	34.06	65.94
g–C₃N₄ 450	9.189	0.08	5.7	2.59	36.00	64.00
g–C₃N₄ 500	13.45	0.092	5.3	2.61	37.00	63.00
g–C₃N₄ 550	48.203	0.32	4.2	2.7	39.3	60.7

Table 1. Surface area, pore volume, crystallite size, band gap and, elemental composition of bulk and exfoliated g–C₃N₄.
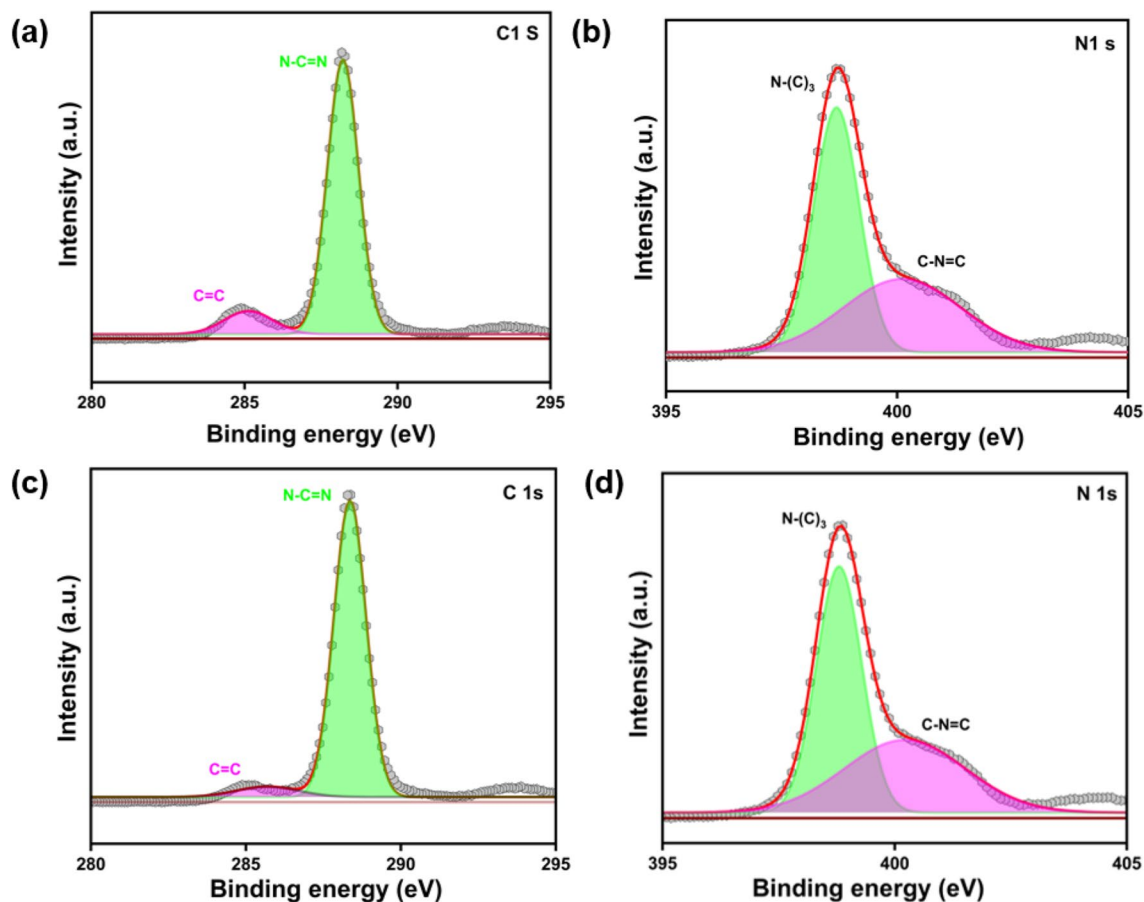
4

Figure 3. XPS spectrum of bulk $g-C_3N_4$ and $g-C_3N_4$ 550. (**a**) C1s spectra of bulk $g-C_3N_4$ (**b**) N1s spectra bulk $g-C_3N_4$, (**c**) C1s spectra for $g-C_3N_4$ 550, (**d**) N1s spectra of $g-C_3N_4$ 550.

were found at 288.34 eV and 285.341. $N-(C)_3$ and $C-N=C$ of N1s were attributed in the range of 398.86 eV and 401.1 eV which confirmed the triazine rings and SP^2 hybridized carbon atom bonded N in the aromatic rings. This also confirmed that the $TE-g-C_3N_4$ had undergone no chemical structural changes in the presence of heat treatment. The survey scan spectrum of bulk $g-C_3N_4$ and $g-C_3N_4$ 550 are shown in Figure S1.

Morphology analysis

Figure 4 illustrated the structural morphology of prepared samples which confirmed the effect of temperature on the thermal exfoliation of the prepared materials. In case of bulk $g-C_3N_4$, flat, aggregated and non-porous flakes were observed while for exfoliated ones, thinner layers with rough surface and layered detachments were found with increasing exfoliation temperature as shown in Fig. 4b–d. There were similar reports in the literature for the exfoliated ones[59,60]. The EDAX analysis confirmed the presence of C and N and their respective percentages as shown in Figure S2. Elemental mapping of prepared samples shown in Figure S3 showed the uniform homogeneous distribution. Furthermore, the elemental composition of all prepared photocatalysts is listed in Table 1.

Surface area analysis

Figure 5 displays the N_2 adsorption–desorption isotherms for the photocatalysts that were produced. The observed samples were determined to conform to the type IV isotherm and exhibited H3 hysteresis loop, consistent with findings described in the existing literature[61]. Moreover, it confirmed that all the prepared samples are multilayer—monolayer adsorption and are mesoporous materials. The specific surface area (S_{BET}) and porosity for prepared samples increased with increasing thermal heat treatment temperature[47]. The specific surface area for $g-C_3N_4$ bulk, $g-C_3N_4$ 450, $g-C_3N_4$ 500, $g-C_3N_4$ 550 are 5.035 m^2/g, 9.189 m^2/g, 13.45 m^2/g and 48.203 m^2/g with pore size distribution in the range of 2–20 nm (Figure S4). The increase in surface area upon increase in exfoliation temperature might be attributed to surface roughness, which was observed in FESEM analysis for the thermally exfoliated samples and it also goes well with XRD results. Furthermore, the specific surface area (S_{BET}) and pore volume was also tabulated in Table 1.

Optical study

The optical characteristics of the produced photocatalysts were examined using ultra-violet diffuse reflectance spectroscopy (UV-DRS). The optical absorption spectra of the prepared samples are shown in Fig. 6a. All the
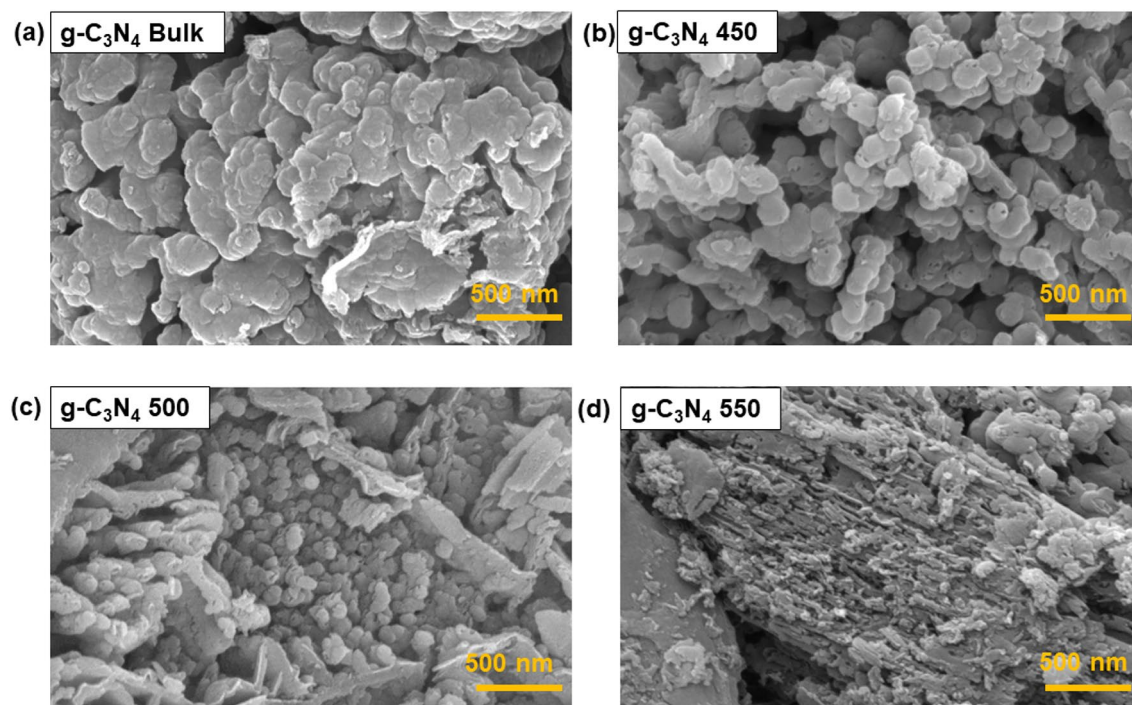
Figure 4. FESEM images of the synthesized samples: (**a**) g–C$_3$N$_4$ Bulk, (**b**) g–C$_3$N$_4$ 450, (**c**) g–C$_3$N$_4$ 500, (**d**) g–C$_3$N$_4$ 550 photocatalyst.
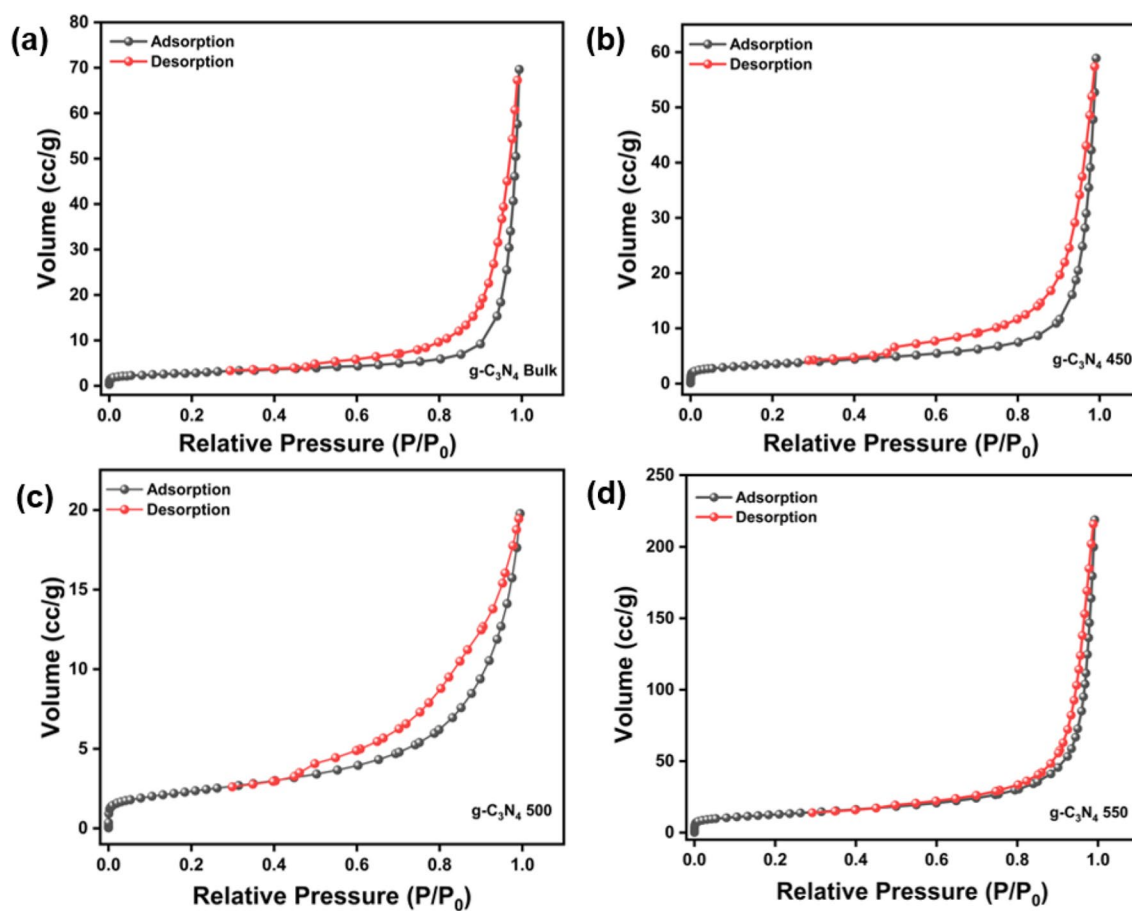
Figure 5. (**a**) N$_2$ adsorption–desorption plots of (**a**) bulk g–C$_3$N$_4$ and, (**b–d**) exfoliated g–C$_3$N$_4$.
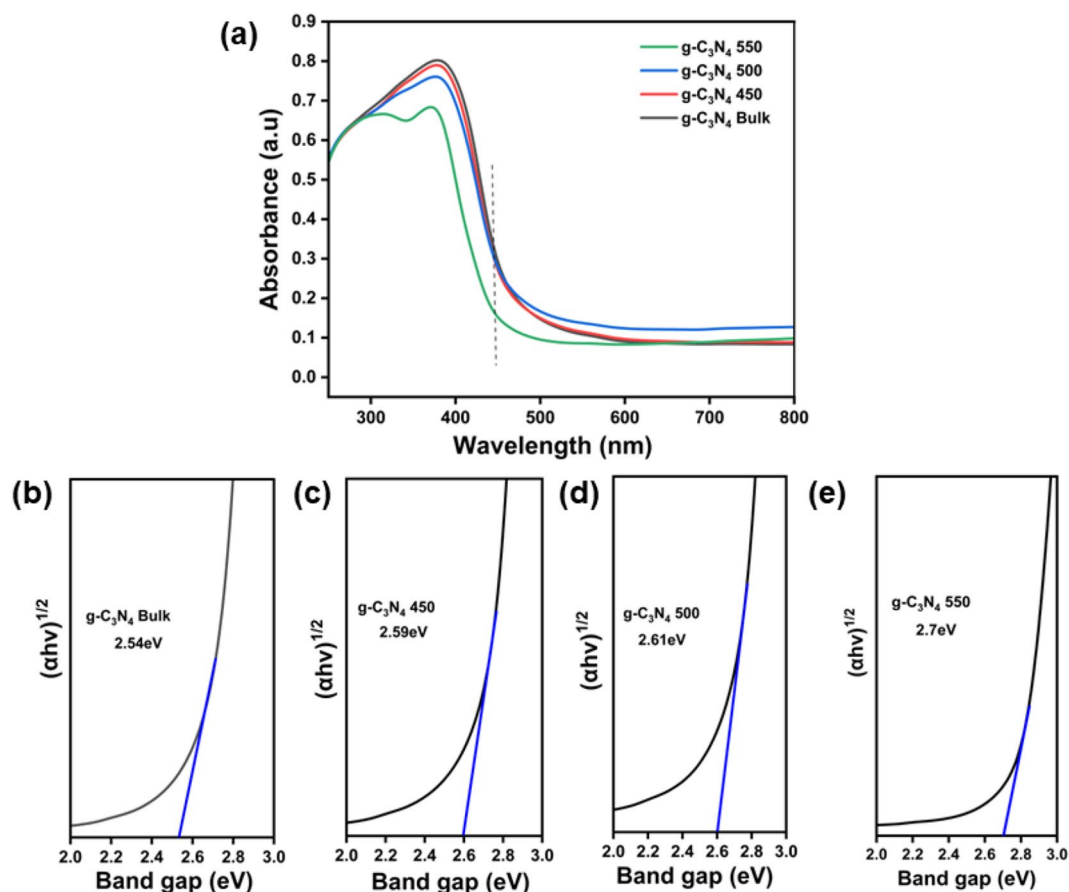
Figure 6. (**a**) UV–Visible absorbance spectra of g–C_3N_4 Bulk, g–C_3N_4 450, g–C_3N_4 500 and g–C_3N_4 550. (**b**–**e**) Band gap analysis-Tauc plot of the prepared samples.

prepared samples exhibited absorption edge at 450 nm depicting intrinsic (π–π^*) transition and showed blue shift after thermal exfoliation because of the quantum confinement effect[62,63]. Moreover, the band gap energies of the catalyst were determined using the tauc equation, and these values are illustrated in the Fig. 6b–e. The band gap energy of prepared samples increased with increasing thermal exfoliation temperature, which further confirmed the quantum confinement effect because of reduction in thickness of exfoliated photocatalysts[64].

Furthermore, the band gaps of all photocatalysts are tabulated in Table 1. The band gap values were calculated using the following equation:

$$\text{Tauc plot}: \alpha h\nu = A\left(h\nu - E_g\right)^{1/2} \tag{3}$$

where, α-absorption coefficient, A-Proportionality constant, h-Planck's constant, ν-photons' frequency, E_g-Bandgap.

Photocatalytic activity

The photocatalytic performance of g–C_3N_4 bulk, g–C_3N_4 450, g–C_3N_4 500, and g–C_3N_4 550 was assessed in relation to the degradation of organic dyes: MB, MO and, RhB, individually. Also, the adsorption efficiencies for both the bulk and exfoliated photocatalysts were studied in the absence of light. Figure S5 showed an increased adsorption efficiency for all the thermally exfoliated samples when compared to the bulk ones. This could be due to increased surface area for the exfoliated samples as confirmed by BET studies. Also, the photodegradation efficiency of prepared photocatalysts could be arranged in the following sequence: g–C_3N_4 bulk< g–C_3N_4 450 < g–C_3N_4 500 < g–C_3N_4 550. The photodegradation efficiency of g–C_3N_4 550 against MB, MO and RhB dyes were found to be 92 ± 0.18%, 93 ± 0.31%, and 95 ± 0.4% respectively within 60 min of UV light irradiation.

Effect of catalyst

The catalytic properties of the prepared catalysts were analyzed by performing photodegradation of all three dyes individually under irradiation of UV light. Initially, all the dyes were kept in the photocatalytic reaction chamber and irradiated for 60 min without a catalyst and their corresponding absorbance spectrum was recorded as shown in Fig. 7a–f. The blank test (black line in Fig. 7) showed no degradation of dyes. However, after addition of photocatalyst to the dye solutions, there was a remarkable reduction in the concentrations of all dye solutions. Figure 7a–c depicted the photocatalytic degradation of three dyes with irradiation time corresponding to the
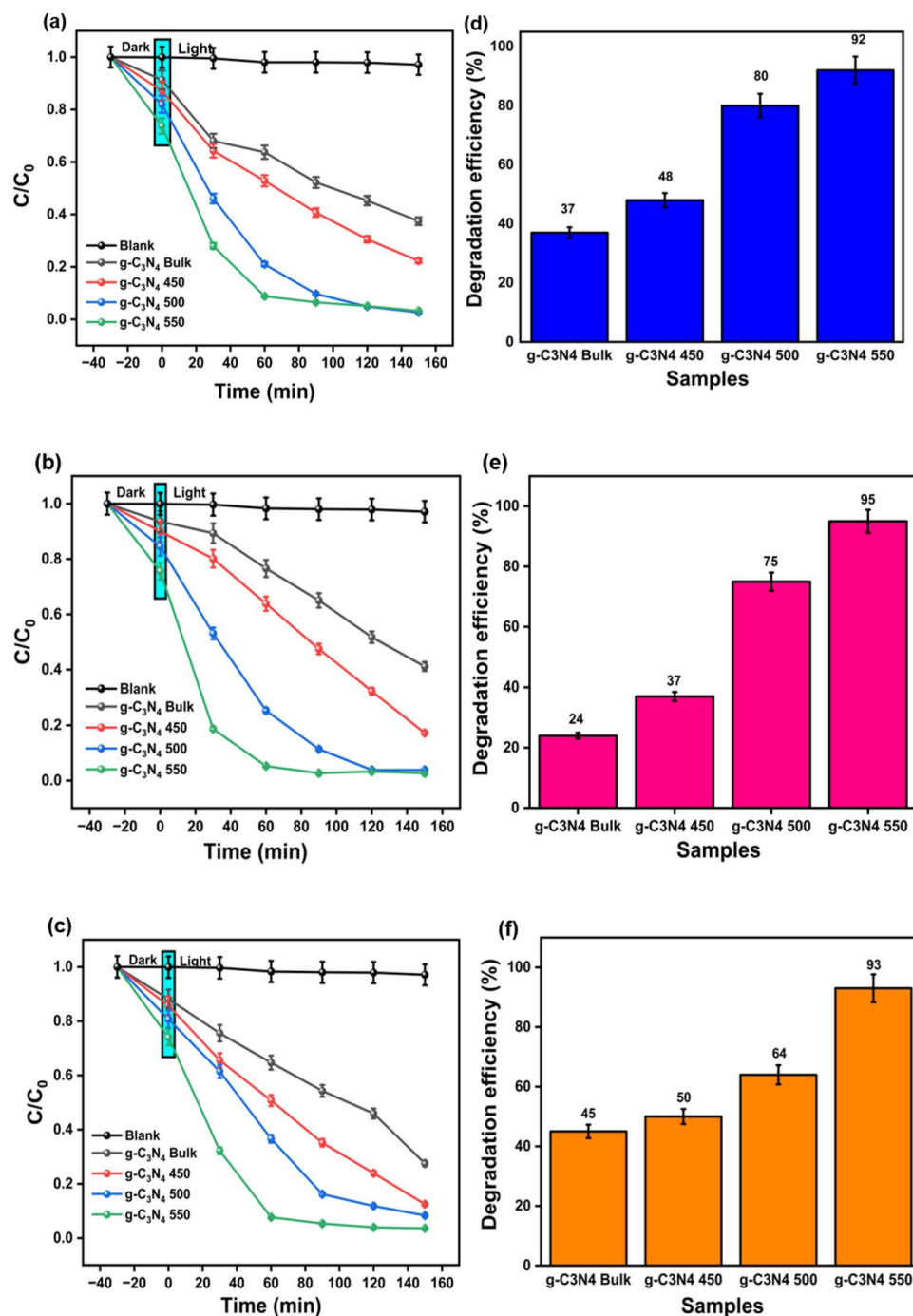
7

Figure 7. (**a**–**c**) Time dependent degradation kinetics measured as the concentration of dye at time t with respect to initial concentration (C/C$_0$), (**d**–**f**) photocatalytic degradation efficiency of all the samples after 60 min of degradation.

C/C$_0$ in all prepared photocatalyst g–C$_3$N$_4$ bulk, g–C$_3$N$_4$ 450, g–C$_3$N$_4$ 500, g–C$_3$N$_4$ 550. Figure 7d–f showed the degradation efficiency of all reported catalysts for all three dyes. The degradation kinetics of three dyes were fitted with first-order rate model. The rate constant values were calculated with the help of Eq. (2) mentioned in section "Photocatalytic experiments".

Moreover, the rate constant for g–C$_3$N$_4$ 550 is higher in all three dye degradation experiments shown as shown in Table 2.

Photocatalyst	MB dye	RhB dye	MO dye
bulk g–C_3N_4	5.39×10^{-3} s^{-1}	4.95×10^{-3} s^{-1}	6.55×10^{-3} s^{-1}
g–C_3N_4 450	8.24×10^{-3} s^{-1}	9.35×10^{-3} s^{-1}	1.120×10^{-2} s^{-1}
g–C_3N_4 500	2.005×10^{-2} s^{-1}	2.086×10^{-2} s^{-1}	1.502×10^{-2} s^{-1}
g–C_3N_4 550	2.133×10^{-2} s^{-1}	2.276×10^{-2} s^{-1}	2.096×10^{-2} s^{-1}

Table 2. Rate constant values for the bulk and exfoliated g-C_3N_4.

Investigation of the photocatalytic reaction mechanisms

Photoluminescence (PL) Spectroscopy and EIS analysis

A good photocatalyst are expected to have high charge transfer rate and low recombination rate of photoexcited holes and electrons[42,65]. PL study and EIS Nyquist plot were used to investigate the catalyst charge carrier recombination effect and charge transfer resistance. PL study was performed to find the recombination rate of photogenerated electron–hole pair of the prepared materials. A wavelength of 400–600 nm was used to examine the emission spectrum of the bulk and exfoliated g–C_3N_4. Figure 8a showed the PL spectra of all catalysts and the peak intensity revealed the recombination rate of photoexcited holes and electrons. In all the catalysts, the peak at 450 nm confirmed the π−π* transitions[66]. The lower intensity for g–C_3N_4 550 indicated the low electron–hole recombination rate, Moreover, all the thermally exfoliated samples showed significantly decreased intensity compared with g–C_3N_4 bulk, confirming the suppression of charge recombination in thermally exfoliated samples. The charge transfer resistance kinetics was also investigated by EIS analysis. Figure 8b showed the EIS Nyquist plots in which g–C_3N_4 550 exhibited a much smaller arc radius suggesting a higher charge transfer rate than g–C_3N_4 bulk and other thermally exfoliated samples.

Radical scavenging tests

In a typical photocatalytic degradation process, the photo-induced hole (h^+), hydroxyl radical (·OH), and superoxide radical (·O_2^-) played a vital role in the degradation of organic pollutants. Thus, it is imperative to identify the most reactive species that enabled the degradation of dyes. As shown in Fig. 9a, without the addition of any scavengers, there was no significant change in the degradation efficiency for all the three dyes. However, in the presence of scavenger para-benzoquinone (P–BQ), there was a significant drop in the degradation efficiency, indicating the superoxide radical to be very important for the degradation of the dyes. Next to P–BQ, there was a slight reduction in the degradation efficiency for all dyes in case of AO ($p = 0.0038$) which indicated that the photoinduced holes also contributed to the catalytic reaction but in a minimal way. There was no significant change ($p = 0.8338$) in the degradation efficiency upon addition of IPA, indicating the poor contribution of hydroxyl radicals towards the photocatalytic reaction. This also goes well with reported literature citing the fact that the valance band edge around + 1.8 eV of g–C_3N_4 is energetically unfulfilled for generation of ·OH[67]. To further confirm the same and to understand the nature of active species involved in the photodegradation, the band position of each catalyst was measured. The positions of the conduction band (CB) and valance band (VB) of the prepared catalyst were determined, and listed in Table 3 using the following empirical formula:

$$E_{CB} = X - E^e - 0.5\,E_g \tag{4}$$

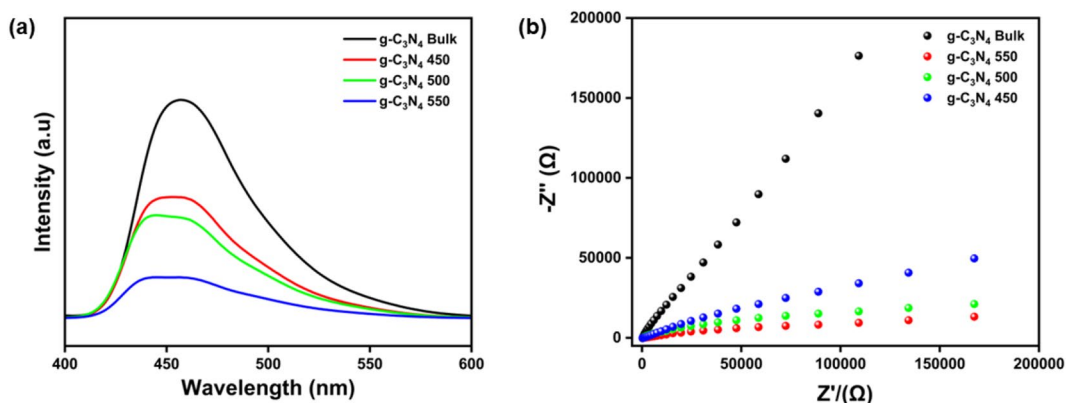$$E_{VB} = E_{CB} + E_g \tag{5}$$

Figure 8. (**a**) Photoluminescence (PL) spectra of prepared photocatalysts, (**b**) EIS analysis of the prepared photocatalysts.
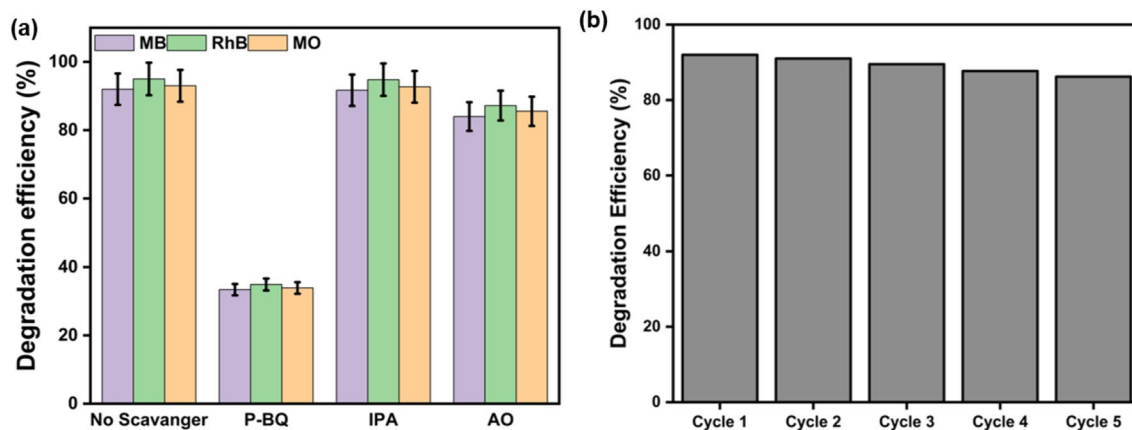
Figure 9. (**a**) Radical scavenging study to determine the reaction mechanisms for g–C$_3$N$_4$ 550 catalysts against three textile dyes. Superoxide anions, hydroxyl radicals and photoinduced hole are quenched by para-benzoquinone (P–BQ), isopropyl alcohol (IPA) and ammonium oxalate (AO), respectively. (**b**) Reusability analysis of g–C$_3$N$_4$ 550 catalysts for five successive cycles.

Photocatalyst	Band gap (eV)	Conduction band potential (eV) [E$_{CB}$]	Valance band potential (eV) [E$_{VB}$]
bulk g–C$_3$N$_4$	2.54	− 1.05	1.49
g–C$_3$N$_4$ 450	2.59	− 1.075	1.51
g–C$_3$N$_4$ 500	2.61	− 1.085	1.52
g–C$_3$N$_4$ 550	2.7	− 1.13	1.57

Table 3. Band gap (E$_g$) and band potentials (E$_{CB}$, E$_{VB}$) of TE- g-C$_3$N$_4$.

where, *X*—absolute electronegativity of the material. For g–C$_3$N$_4$ is 4.72 eV[68]. E^e—energy of free electrons on the hydrogen scale (E^e = 4.5 eV), E$_{CB}$—conduction band potential, E$_{VB}$—valance band potential.

Additionally, Mott-Schottky analysis was also performed for the best catalyst g-C$_3$N$_4$ 550, which were used for the scavenging study to confirm the conduction band potential (E$_{CB}$). The flat band potential (V$_{fb}$) for the catalyst was calculated as − 1.21 eV using the Mott-Schottky plot with respect to Ag/AgCl as reference electrode as shown in Figure S6. In general, for n-type semiconductor catalyst V$_{fb}$ is ∼ 0.1 eV more negative than E$_{CB}$[69]. Thus, E$_{CB}$ for g–C$_3$N$_4$ was calculated to be ∼ − 1.1 eV, and E$_{VB}$ was found to be 1.6 eV. This result agreed with the results from the reported literature[67,70]. The proposed photocatalytic mechanism of TE–g–C$_3$N$_4$ was illustrated in the Fig. 10.

Evaluation of the reusability of the photocatalysts

The best-performing g–C$_3$N$_4$ 550 was tested for its stability and reusability for five continuous cycles with MB dye. Figure 9b showed the results for the reusability cycle experiments of the photocatalysts. It was interesting to find that only very slight decline in the degradation efficiency of the photocatalyst after 5 continuous cycles from around 92–86.2%. This slight decline might also be due to the loss of photocatalytic materials due to centrifugation process that was collected after each cycle. Additionally, post reusability of g–C$_3$N$_4$ 550 catalysts was analysed with XRD and FTIR which did not show any significant changes in in the spectra as shown in Figure S7. This test confirmed the reusability of prepared photocatalysts, which was very important for translating this technology to more practical applications.

Conclusion

The TE–g–C$_3$N$_4$ was synthesized by subjecting the bulk g–C$_3$N$_4$ to high temperatures and found that g–C$_3$N$_4$ exfoliated at 550 °C showed better photocatalytic degradation efficiency in comparison with its bulk counterparts as well as catalysts synthesized at other lower temperatures. TE–g–C$_3$N$_4$ were observed to be porous and have rough surfaces resulting in high surface area as measured using BET, and SEM analysis. Due to increased specific surface area (48.203 m^2/g), and band gap (2.7 eV), the results noticed for g–C$_3$N$_4$ 550 against MB, MO and RhB dyes were found to be 92 ± 0.18%, 93 ± 0.31%, and 95 ± 0.4% respectively in 60 min of light irradiation and all these results followed first-order rate kinetics. In a radical scavenging study, it was found that the superoxide radicals played a crucial role in the photocatalytic degradation reaction followed by photogenerated holes in a very minimal way. However, further investigations on the in-depth mechanisms of how holes contribute to the degradation of dyes are warranted. Furthermore, the EIS and PL study confirmed the charge transfer ability and carrier recombination effect which further confirmed that the efficiency of the catalyst improved in the following sequence: g–C$_3$N$_4$ bulk < g–C$_3$N$_4$ 450 < g–C$_3$N$_4$ 500 < g–C$_3$N$_4$ 550. The reusability studies on the best performing photocatalyst confirmed its excellent reusability with minor decrease in activity from 92 to 86.2%
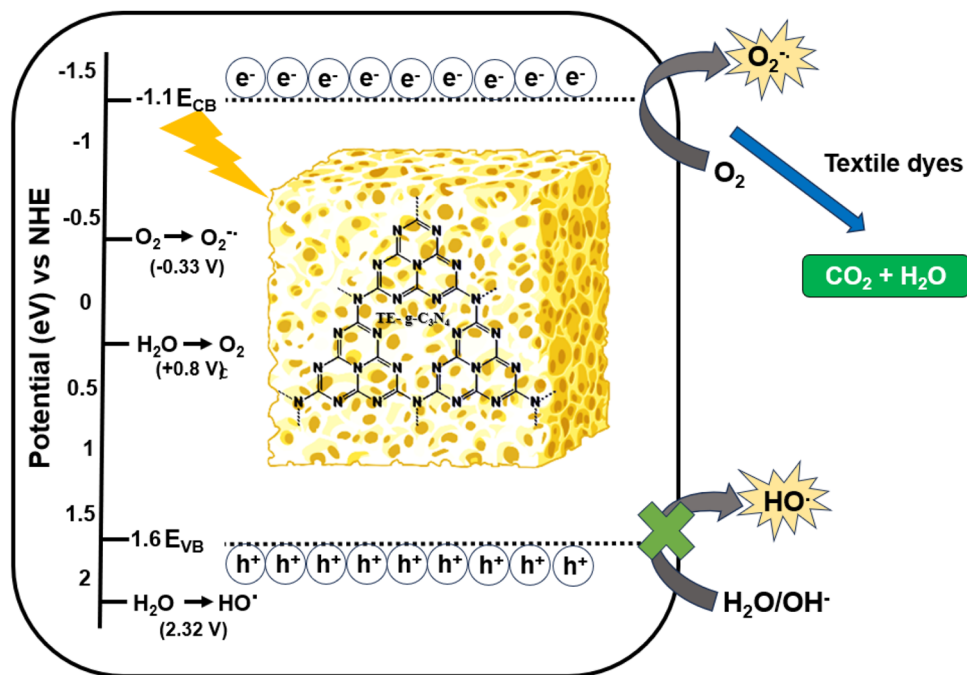
Figure 10. The proposed photocatalytic reaction mechanism of TE–g–C_3N_4 against textile dye pollutants.

after 5 consecutive runs. Thus, TE–g–C_3N_4 could be a potential green photocatalyst which could be deployed in the wastewater treatment applications after a few further pilot scale investigations.

Data availability

All data that supports the findings of the study are available from the corresponding author on reasonable request.

References

1. Khairul Akter, M. M., Haq, U. N., Islam, M. M. & Uddin, M. A. Textile-apparel manufacturing and material waste management in the circular economy: A conceptual model to achieve sustainable development goal (SDG) 12 for Bangladesh. *Clean. Environ. Syst.* **4**, 100070. https://doi.org/10.1016/j.cesys.2022.100070 (2022).
2. Akhtar, W. H., Watanabe, C., Tou, Y. & Neittaanmäki, P. A new perspective on the textile and apparel industry in the digital transformation era. *Textiles* **2**, 633–656 (2022).
3. Luján-Ornelas, C., Güereca, L. P., Franco-García, M.-L. & Heldeweg, M. A life cycle thinking approach to analyse sustainability in the textile industry: A literature review. *Sustainability* **12**, 10193 (2020).
4. Berradi, M. *et al.* Textile finishing dyes and their impact on aquatic environs. *Heliyon* **5**, e02711. https://doi.org/10.1016/j.heliyon.2019.e02711 (2019).
5. Tamburini, D., Shimada, C. M. & McCarthy, B. T. The molecular characterization of early synthetic dyes in E. Knecht's textile sample book "A Manual of Dyeing", (1893) by high performance liquid chromatography-diode array detector-mass spectrometry (HPLC-DAD-MS). *Dyes Pigments* **190**, 109286. https://doi.org/10.1016/j.dyepig.2021.109286 (2021).
6. Slama, H. B. *et al.* Diversity of synthetic dyes from textile industries, discharge impacts and treatment methods. *Appl. Sci.* **11**, 6255 (2021).
7. Niinimäki, K. *et al.* The environmental price of fast fashion. *Nat. Rev. Earth Environ.* **1**, 189–200. https://doi.org/10.1038/s43017-020-0039-9 (2020).
8. Paul, D. Research on heavy metal pollution of river Ganga: A review. *Ann. Agrar. Sci.* **15**, 278–286. https://doi.org/10.1016/j.aasci.2017.04.001 (2017).
9. Dwivedi, S., Mishra, S. & Tripathi, R. D. Ganga water pollution: A potential health threat to inhabitants of Ganga basin. *Environ. Int.* **117**, 327–338. https://doi.org/10.1016/j.envint.2018.05.015 (2018).
10. Low, J., Cao, S., Yu, J. & Wageh, S. Two-dimensional layered composite photocatalysts. *Chem. Commun.* **50**, 10768–10777. https://doi.org/10.1039/C4CC02553A (2014).
11. Khan, I. *et al.* Review on methylene blue: Its properties, uses toxicity and photodegradation. *Water* **14**, 242 (2022).
12. Hassan, M. M. & Carr, C. M. A critical review on recent advancements of the removal of reactive dyes from dyehouse effluent by ion-exchange adsorbents. *Chemosphere* **209**, 201–219. https://doi.org/10.1016/j.chemosphere.2018.06.043 (2018).
13. Sharma, J., Sharma, S. & Soni, V. Classification and impact of synthetic textile dyes on aquatic flora: A review. *Reg. Stud. Mar. Sci.* **45**, 101802. https://doi.org/10.1016/j.rsma.2021.101802 (2021).
14. Al-Tohamy, R. *et al.* A critical review on the treatment of dye-containing wastewater: Ecotoxicological and health concerns of textile dyes and possible remediation approaches for environmental safety. *Ecotoxicol. Environ. Saf.* **231**, 113160. https://doi.org/10.1016/j.ecoenv.2021.113160 (2022).
15. Lellis, B., Fávaro-Polonio, C. Z., Pamphile, J. A. & Polonio, J. C. Effects of textile dyes on health and the environment and bioremediation potential of living organisms. *Biotechnol. Res. Innov.* **3**, 275–290. https://doi.org/10.1016/j.biori.2019.09.001 (2019).

16. Nilsson, R., Nordlinder, R., Wass, U., Meding, B. & Belin, L. Asthma, rhinitis, and dermatitis in workers exposed to reactive dyes. *Br. J. Ind. Med.* **50**, 65–70. https://doi.org/10.1136/oem.50.1.65 (1993).

17. Kooter, I. *et al.* Molecular signature of asthma-enhanced sensitivity to CuO nanoparticle aerosols from 3D cell model. *ACS Nano* **13**, 6932–6946. https://doi.org/10.1021/acsnano.9b01823 (2019).

18. Adane, T., Adugna, A. T. & Alemayehu, E. Textile industry effluent treatment techniques. *J. Chem.* **2021**, 5314404. https://doi.org/10.1155/2021/5314404 (2021).

19. Ismail, W. *et al.* Water treatment and artificial intelligence techniques: A systematic literature review research. *Environ. Sci. Pollut. Res.* **30**, 71794–71812. https://doi.org/10.1007/s11356-021-16471-0 (2023).

20. Sikosana, M. L., Sikhwivhilu, K., Moutloali, R. & Madyira, D. M. Municipal wastewater treatment technologies: A review. *Proc. Manuf.* **35**, 1018–1024. https://doi.org/10.1016/j.promfg.2019.06.051 (2019).

21. Rani, B., Nayak, A. K. & Sahu, N. K. *Nanostructured Materials for Visible Light Photocatalysis* 1–22 (Elsevier, 2022).

22. Ren, G. *et al.* Recent advances of photocatalytic application in water treatment: A review. *Nanomaterials* **11**, 1804 (2021).

23. Chong, M. N., Jin, B., Chow, C. W. K. & Saint, C. Recent developments in photocatalytic water treatment technology: A review. *Water Res.* **44**, 2997–3027. https://doi.org/10.1016/j.watres.2010.02.039 (2010).

24. Schneider, J. *et al.* Understanding TiO₂ photocatalysis: Mechanisms and materials. *Chem. Rev.* **114**, 9919–9986. https://doi.org/10.1021/cr5001892 (2014).

25. Rajbongshi, B. M. *Handbook of Smart Photocatalytic Materials* 127–149 (Elsevier, 2020).

26. Yang, X. & Wang, D. Photocatalysis: From fundamental principles to materials and applications. *ACS Appl. Energy Mater.* **1**, 6657–6693. https://doi.org/10.1021/acsaem.8b01345 (2018).

27. Porley, V. & Robertson, N. *Nanostructured Photocatalysts* 129–171 (Elsevier, 2020).

28. Ong, W.-J., Tan, L.-L., Ng, Y. H., Yong, S.-T. & Chai, S.-P. Graphitic carbon nitride (g–C3N4)-based photocatalysts for artificial photosynthesis and environmental remediation: Are we a step closer to achieving sustainability?. *Chem. Rev.* **116**, 7159–7329. https://doi.org/10.1021/acs.chemrev.6b00075 (2016).

29. Li, H., Liu, Y., Gao, X., Fu, C. & Wang, X. Facile synthesis and enhanced visible-light photocatalysis of graphitic carbon nitride composite semiconductors. *ChemSusChem* **8**, 1189–1196. https://doi.org/10.1002/cssc.201500024 (2015).

30. Chen, Y. *et al.* Surface modification of g–C3N4 by hydrazine: Simple way for noble-metal free hydrogen evolution catalysts. *Chem. Eng. J.* **286**, 339–346. https://doi.org/10.1016/j.cej.2015.10.080 (2016).

31. Jürgens, B. *et al.* Melem (2,5,8-Triamino-tri-s-triazine), an important intermediate during condensation of melamine rings to graphitic carbon nitride: Synthesis, structure determination by X-ray powder diffractometry, solid-state NMR, and theoretical studies. *J. Am. Chem. Soc.* **125**, 10288–10300. https://doi.org/10.1021/ja0357689 (2003).

32. Komatsu, T. & Nakamura, T. Polycondensation/pyrolysis of tris-s-triazine derivatives leading to graphite-like carbon nitrides. *J. Mater. Chem.* **11**, 474–478. https://doi.org/10.1039/B005982J (2001).

33. Xia, P., Zhu, B., Cheng, B., Yu, J. & Xu, J. 2D/2D g-C3N4/MnO2 nanocomposite as a direct Z-scheme photocatalyst for enhanced photocatalytic activity. *ACS Sustain. Chem. Eng.* **6**, 965–973. https://doi.org/10.1021/acssuschemeng.7b03289 (2018).

34. Chen, Y. & Bai, X. A review on quantum dots modified g-C3N4-Based photocatalysts with improved photocatalytic activity. *Catalysts* **10**, 142 (2020).

35. Alaghmandfard, A. & Ghandi, K. A comprehensive review of graphitic carbon nitride (g-C3N4)–metal oxide-based nanocomposites: Potential for photocatalysis and sensing. *Nanomaterials* **12**, 294 (2022).

36. Alam, U., Pandey, K. & Verma, N. Photocatalytic oxidation of glyphosate and reduction of Cr(VI) in water over ACF-supported CoNiWO4-gCN composite under batch and flow conditions. *Chemosphere* **297**, 134119. https://doi.org/10.1016/j.chemosphere.2022.134119 (2022).

37. Alam, U., Pandey, A. & Verma, N. An anthraquinone-integrated S-scheme-based NiTiO₃-g-C₃N₄ composite with enhanced hydrogen production activity. *Int. J. Hydrog. Energy* **48**, 2532–2541. https://doi.org/10.1016/j.ijhydene.2022.10.151 (2023).

38. Beyhaqi, A., Azimi, S. M. T., Chen, Z., Hu, C. & Zeng, Q. Exfoliated and plicated g-C₄N₄ nanosheets for efficient photocatalytic organic degradation and hydrogen evolution. *Int. J. Hydrog. Energy* **46**, 20547–20559. https://doi.org/10.1016/j.ijhydene.2021.03.174 (2021).

39. Feng, J. *et al.* Comparing the photocatalytic properties of g–C3N4 treated by thermal decomposition, solvothermal and protonation. *Results Phys.* **11**, 331–334. https://doi.org/10.1016/j.rinp.2018.09.014 (2018).

40. Huang, T. *et al.* General synthesis strategy for hollow porous prismatic graphitic carbon nitride: A high-performance photocatalyst for H₂ production and degradation of RhB. *J. Mater. Sci.* **55**, 6037–6050. https://doi.org/10.1007/s10853-020-04439-3 (2020).

41. Rani, B., Nayak, A. K. & Sahu, N. K. Degradation of mixed cationic dye pollutant by metal free melem derivatives and graphitic carbon nitride. *Chemosphere* **298**, 134249. https://doi.org/10.1016/j.chemosphere.2022.134249 (2022).

42. Wang, H. *et al.* Self-assembled sulphur doped carbon nitride for photocatalytic water reforming of methanol. *Chem. Eng. J.* **445**, 136790. https://doi.org/10.1016/j.cej.2022.136790 (2022).

43. Papailias, I. *et al.* Effect of processing temperature on structure and photocatalytic properties of g–C3N4. *Appl. Surf. Sci.* **358**, 278–286. https://doi.org/10.1016/j.apsusc.2015.08.097 (2015).

44. Papailias, I. *et al.* Chemical vs thermal exfoliation of g-C₃N₄ for NOx removal under visible light irradiation. *Appl. Catal. B Environ.* **239**, 16–26. https://doi.org/10.1016/j.apcatb.2018.07.078 (2018).

45. Hwa, K.-Y., Santhan, A., Ganguly, A. & Kanna Sharma, T. S. Two dimensional architectures of graphitic carbon nitride with the substitution of heteroatoms for bifunctional electrochemical detection of nilutamide. *Chemosphere* **320**, 138068. https://doi.org/10.1016/j.chemosphere.2023.138068 (2023).

46. Chellammal Gayathri, R., Elakkiya, V. & Sumathi, S. Synthesis of cerium and bismuth doped nickel aluminate for the photodegradation of methylene blue, methyl orange and rhodamine B dyes. *Chemosphere* **303**, 135056. https://doi.org/10.1016/j.chemosphere.2022.135056 (2022).

47. Niu, P., Zhang, L., Liu, G. & Cheng, H.-M. Graphene-like carbon nitride nanosheets for improved photocatalytic activities. *Adv. Funct. Mater.* **22**, 4763–4770. https://doi.org/10.1002/adfm.201200922 (2012).

48. Zhang, J., Zhang, M., Yang, C. & Wang, X. Nanospherical carbon nitride frameworks with sharp edges accelerating charge collection and separation at a soft photocatalytic interface. *Adv. Mater.* **26**, 4121–4126. https://doi.org/10.1002/adma.201400573 (2014).

49. Yang, S. *et al.* Exfoliated graphitic carbon nitride nanosheets as efficient catalysts for hydrogen evolution under visible light. *Adv. Mater.* **25**, 2452–2456. https://doi.org/10.1002/adma.201204453 (2013).

50. Yang, L. *et al.* A surface modification resultant thermally oxidized porous g–C₃N₄ with enhanced photocatalytic hydrogen production. *Appl. Catal. B Environ.* **204**, 335–345. https://doi.org/10.1016/j.apcatb.2016.11.047 (2017).

51. Xu, H.-Y., Zheng, Z. & Mao, G.-J. Enhanced photocatalytic discoloration of acid fuchsine wastewater by TiO₂/schorl composite catalyst. *J. Hazard. Mater.* **175**, 658–665. https://doi.org/10.1016/j.jhazmat.2009.10.059 (2010).

52. Song, X., Yang, Q., Jiang, X., Yin, M. & Zhou, L. Porous graphitic carbon nitride nanosheets prepared under self-producing atmosphere for highly improved photocatalytic activity. *Appl. Catal. B Environ.* **217**, 322–330. https://doi.org/10.1016/j.apcatb.2017.05.084 (2017).

53. Gupta, R., Alam, U. & Verma, N. Efficient photofixation of nitrogen to ammonia over an S-scheme-based NiSnO₃–g–C₃N₄ heterojunction. *Chem. Eng. J.* **479**, 147644. https://doi.org/10.1016/j.cej.2023.147644 (2024).

54. Qu, Y. & Duan, X. Progress, challenge and perspective of heterogeneous photocatalysts. *Chem. Soc. Rev.* **42**, 2568–2580. https://doi.org/10.1039/C2CS35355E (2013).

55. Samanta, S., Martha, S. & Parida, K. Facile synthesis of Au/g-C3N4 nanocomposites: An inorganic/organic hybrid plasmonic photocatalyst with enhanced hydrogen gas evolution under visible-light irradiation. *ChemCatChem* **6**, 1453–1462. https://doi.org/10.1002/cctc.201300949 (2014).

56. Kang, Y. *et al.* An amorphous carbon nitride photocatalyst with greatly extended visible-light-responsive range for photocatalytic hydrogen generation. *Adv. Mater.* **27**, 4572–4577. https://doi.org/10.1002/adma.201501939 (2015).

57. Li, Q., He, Y. & Peng, R. Graphitic carbon nitride (g-C3N4) as a metal-free catalyst for thermal decomposition of ammonium perchlorate. *RSC Adv.* **5**, 24507–24512. https://doi.org/10.1039/C5RA01157D (2015).

58. Xue, J., Ma, S., Zhou, Y., Zhang, Z. & He, M. Facile photochemical synthesis of Au/Pt/g–C3N4 with plasmon-enhanced photocatalytic activity for antibiotic degradation. *ACS Appl. Mater. Interfaces* **7**, 9630–9637. https://doi.org/10.1021/acsami.5b01212 (2015).

59. Kong, L. *et al.* Porous size dependent g–C3N4 for efficient photocatalysts: Regulation synthesizes and physical mechanism. *Mater. Today Energy* **13**, 11–21. https://doi.org/10.1016/j.mtener.2019.04.011 (2019).

60. Phoon, B. L., Lai, C. W., Pan, G.-T., Yang, T.C.-K. & Juan, J. C. Highly mesoporous g–C3N4 with uniform pore size distribution via the template-free method to enhanced solar-driven tetracycline degradation. *Nanomaterials* **11**, 2041 (2021).

61. Monga, D. & Basu, S. Enhanced photocatalytic degradation of industrial dye by g–C3N4/TiO2 nanocomposite: Role of shape of TiO2. *Adv. Powder Technol.* **30**, 1089–1098. https://doi.org/10.1016/j.apt.2019.03.004 (2019).

62. Wang, K. *et al.* Sulfur-doped g–C3N= with enhanced photocatalytic CO2-reduction performance. *Appl. Catal. B Environ.* **176–177**, 44–52. https://doi.org/10.1016/j.apcatb.2015.03.045 (2015).

63. Saravanakumar, K. & Park, C. M. Rational design of a novel LaFeO3/g-C3N4/BiFeO3 double Z-scheme structure: Photocatalytic performance for antibiotic degradation and mechanistic insight. *Chem. Eng. J.* **423**, 130076. https://doi.org/10.1016/j.cej.2021.130076 (2021).

64. Liang, L. *et al.* g–C3N4 nano-fragments as highly efficient hydrogen evolution photocatalysts: Boosting effect of nitrogen vacancy. *Appl. Catal. A Gen.* **599**, 117618. https://doi.org/10.1016/j.apcata.2020.117618 (2020).

65. Devi, L. G. & Kavitha, R. A review on non metal ion doped titania for the photocatalytic degradation of organic pollutants under UV/solar light: Role of photogenerated charge carrier dynamics in enhancing the activity. *Appl. Catal. B Environ.* **140–141**, 559–587. https://doi.org/10.1016/j.apcatb.2013.04.035 (2013).

66. Yuan, X. *et al.* Facile synthesis of 3D porous thermally exfoliated g–C3N4 nanosheet with enhanced photocatalytic degradation of organic dye. *J. Coll. Interface Sci.* **468**, 211–219. https://doi.org/10.1016/j.jcis.2016.01.048 (2016).

67. Liu, N. *et al.* From Triazine to Heptazine: Origin of graphitic carbon nitride as a photocatalyst. *ACS Omega* **5**, 12557–12567. https://doi.org/10.1021/acsomega.0c01607 (2020).

68. Jia, T. *et al.* Rational construction of direct Z-scheme SnS/g-C3N4 hybrid photocatalyst for significant enhancement of visible-light photocatalytic activity. *Appl. Surf. Sci.* **499**, 143941. https://doi.org/10.1016/j.apsusc.2019.143941 (2020).

69. Bahadoran, A. *et al.* Novel S-scheme WO3/CeO2 heterojunction with enhanced photocatalytic degradation of sulfamerazine under visible light irradiation. *Appl. Surf. Sci.* **568**, 150957. https://doi.org/10.1016/j.apsusc.2021.150957 (2021).

70. Xu, J., Wang, Z. & Zhu, Y. Enhanced Visible-light-driven photocatalytic disinfection performance and organic pollutant degradation activity of porous g–C3N4 nanosheets. *ACS Appl. Mater. Interfaces* **9**, 27727–27735. https://doi.org/10.1021/acsami.7b07657 (2017).

Acknowledgements

Author contributions

S.G: Synthesis, Methodology, Conceptualization, Data curation, Formal analysis, Investigation, Writing—original draft. T.K: Formal analysis, Visualization. S.S: Conceptualization, Resource, Formal analysis. A.P: Supervision, Resources, Data curation, Funding acquisition, Conceptualization, Validation, Writing—review & editing.

Competing interests

The authors declare no competing interests.

Additional information

Supplementary Information The online version contains supplementary material available at https://doi.org/10.1038/s41598-024-52688-y.

Correspondence and requests for materials should be addressed to A.P.

Reprints and permissions information is available at www.nature.com/reprints.

Publisher's note Springer Nature remains neutral with regard to jurisdictional claims in published maps and institutional affiliations.